Research Square

Preprints are preliminary reports that have not undergone peer review.
They should not be considered conclusive, used to inform clinical practice,
or referenced by the media as validated information.

Polarization-encoded multifocal stitching imaging based on all-dielectric metasurface engineering

Jiajing He

jiajinghe@siom.ac.cn

Shanghai Institute of optics and fine mechanics, Chinese academy of science https://orcid.org/0000-0002-6477-1061

Xiaojie Sun

Shanghai Institute of optics and fine mechanics, Chinese academy of science

xuan yang

Shanghai Institute of Optics and Fine Mechanics Chinese Academy of Sciences

Haiyang Song

Shanghai Institute of optics and fine mechanics, Chinese academy of science

Haixu Tao

Shanghai Institute of optics and fine mechanics, Chinese academy of science

Jingpei Cai

School of Microelectronics, Shanghai University

Jiaxuan Zou

Shanghai Institute of optics and fine mechanics, Chinese academy of science

Long Zhang

Shanghai Institute of Optics and Fine Mechanics

Jun Wang

Shanghai Institute of Optics and Fine Mechanics, Chinese Academy of Sciences
https://orcid.org/0000-0003-0064-3551

Article

Keywords: metalens, polarization encoding, multifocal imaging

Posted Date: November 13th, 2026

DOI: https://doi.org/10.21203/rs.3.rs-11430571/v1

License: This work is licensed under a Creative Commons Attribution 4.0 International License.
Read Full License

Additional Declarations: There is no conflict of interest

Polarization-encoded multifocal stitching imaging based on all-dielectric metasurface engineering

Xiaojie Sun[1,2], Xuan Yang[1,2,3†], Haiyang Song[1,2], Haixu Tao[1,2], Jingpei Cai[1,2,4], Jiaxuan Zou[1,2], Long Zhang[1,2], Jiajing He[1,2*], and Jun Wang[1,2]

[1] Department of Interdisciplinary Photonics, Shanghai Institute of Optics and Fine Mechanics, Chinese Academy of Sciences, Shanghai 201800, China
[2] Center of Materials Science and Optoelectronics Engineering, University of Chinese Academy of Sciences, Beijing 100049, China
[3] ShanghaiTech University, Shanghai 201210, China
[4] School of Microelectronics, Shanghai University, Shanghai 201800, China
*Corresponding authors. Emails: jiajinghe@siom.ac.cn

Abstract: The development of integrated microscopic imaging requires optical systems to simultaneously possess miniaturization, multi-channel control, and high-quality imaging capabilities, while traditional lens systems still have limitations in terms of structural compactness and functional reuse. This paper presents a polarization-coded multifocal stitching imaging system based on an all-dielectric metalens. By using polarization multiplexing and phase modulation, the designed metalens can achieve selective multifocal modulation of the incident polarization state: it generates 8 focal spots under left-handed circularly polarized light, 4 focal spots under right-handed circularly polarized light, and can simultaneously excite all 12 focal spots under linearly polarized light. The metalens was further used to perform multifocal imaging and stitching reconstruction on a resolution plate, verifying its multi-channel imaging capability. As a proof of principle, based on the experimentally measured multifocal PSF, convolutional coding, demixing, and stitching reconstruction methods were used to perform computational imaging processing on onion epidermal cell images, achieving effective reconstruction of complex biological sample images. This work demonstrates the application potential of polarization-multiplexed metasurfaces in integrated multifocal imaging and computational reconstruction.

Keywords: metalens, polarization encoding, multifocal imaging

Traditional optical microscopy systems typically rely on multiple refractive lenses, polarization elements, and complex optical paths to achieve wavefront modulation, polarization analysis, and target imaging; however, these systems are often bulky, require precise optical alignment, and present challenges for system integration. In recent years, metasurfaces, as two-dimensional optical devices composed of subwavelength artificial micro- and nanostructures, have been able to flexibly control the phase, amplitude, and polarization state of incident light within an ultrathin plane, providing a new technical path for the miniaturization and integration of optical systems[1-3]. Among them, all-dielectric metasurfaces have been widely applied in fields such as metalenses[4,5], beam shaping[6], polarization control[7], and compact imaging[8], owing to their low loss, high transmission efficiency, and strong wavefront manipulation capabilities[9-11]. As a representative application of all-dielectric metasurfaces in the field of imaging, metalenses utilize arrays of sub-wavelength structures to achieve light-field focusing and target imaging. Driven by advancements in micro-

nano fabrication, dispersion engineering, and inverse design methods, metalenses have undergone substantial advances in focusing efficiency, imaging quality, functional integration, and system-level applications, evolving from simple focusing devices into multifunctional planar optical platforms[12-16].

The manipulation of the polarization degree of freedom provides an important means for achieving multifunctional multiplexing in metasurfaces. By designing anisotropic nanostructures, independent phase responses can be obtained for the polarization states of different incident beams, thereby enabling functions such as chiral imaging[17], polarization analysis[18-20], multi-channel holography[21], polarization-selective focusing, and multi-focal point control[22]. In the field of multifocal metalenses, research has already demonstrated functionalities such as polarization-rotation-dependent multifocality[23], helical-direction-dependent multifocality[24], bifocal/trifocal imaging[25,26], multifocal spectral analysis[27], and multifocal beam splitting for polarization detection[28,29]. In recent years, related research has further achieved varifocal metalens microscopy, multifocal image scanning, focus-tunable light-field imaging, and multi-wavelength multifocal designs, demonstrating the potential of multifocal metalenses for parallel light-field manipulation and integrated imaging[30-34]. However, existing research has focused on focal spot generation, energy distribution, polarization beam splitting, or the demonstration of device functionalities, while the mechanisms governing information encoding and reconstruction for multi-focal structures within practical imaging chains remain insufficiently discussed. In the context of multi-focal imaging, the multiple focal spots do not simply correspond to independent imaging channels; rather, they collectively constitute the system's point spread function, leading to spatial overlap and information aliasing among the different focal channels when interacting with actual targets. Therefore, merely verifying the focal-plane spot distribution is insufficient to comprehensively evaluate the device's performance in imaging applications; it is also necessary to further validate the feasibility of multifocal modulation in practical imaging by incorporating measured PSFs and appropriate image reconstruction methods[35-37].

This paper presents a multifocal metalens based on all-dielectric polarization coding and uses a demixing and stitching method to image the target object. The designed metalens generates eight focal spots under left-handed circularly polarized light incidence and four focal spots under right-handed circularly polarized light incidence, while simultaneously producing all twelve focal spots under linearly polarized light incidence. In addition, the focusing performance and polarization selectivity of device were characterized using metrics such as focal-plane light intensity distribution, polarization contrast, PSF, and MTF. Subsequently, an imaging test system was set up to conduct multi-focal imaging experiments on a resolution target, and reconstructed images were obtained by combining unmixing and stitching algorithms. Furthermore, using the experimentally measured 12 focal spot PSF, computational imaging validation was conducted with onion epidermal microscope images serving as complex targets. By integrating polarization multiplexing, multi-focal spot modulation, and computational reconstruction, this work offers a feasible approach for integrated multi-focal-spot microscopy.

Design Principle of the Polarization-Encoded Metalens.

Figure 1(a) shows the schematic diagram of the multifocal metalens based on polarization coding. The unit cell of the polarization-encoded multifocal metalens is illustrated in Figure 1(b). The structure we adopted is amorphous silicon deposited on a fused silica substrate with a thickness of 620 nm. Since amorphous silicon has a high refractive index of 3.29 at a wavelength of 980 nm and an absorption coefficient of 0, it is a good material to choose for near-infrared band design. The designed unit cell has a period P of 600 nm. The metalens was designed and simulated using the finite-difference time-domain (FDTD) method. First, the length and width of the nanostructure were swept under x-polarized light incidence, with a scanning range from 100 nm to 500 nm and a step size of 10 nm. The results for the structural transmittance distribution Tx and phase distribution φ_x for length and width are shown in Figure S1(a) and Figure S1(b) of Supplementary Section 1, respectively. Figure S1(c) presents the polarization conversion efficiency as a function of the length and width. Here, we select the structural parameters with the highest polarization conversion efficiency as the length and width of the meta-atom. The structure has a length of L = 410 nm, a width of W = 170 nm, and a height of H = 620 nm, respectively. The polarization conversion efficiency at this structural size is over 95%. The metalens was fabricated using electron beam lithography, and the detailed fabrication process is provided in Supplementary Section 5. In addition, the fabricated metalens was characterized by scanning electron microscopy (SEM). Figures 1(c) and 1(d) show the top view and 135° tilted view SEM images, respectively. The SEM images indicate that the fabrication error is approximately within 5%.

The proposed metalens is realized through a spin decoupling strategy. Based on the Pancharatnam–Berry (PB) phase design, an additional geometric phase is generated, and an incident circularly polarized beam is converted into the orthogonal circular polarization state after passing through the metasurface. Therefore, the geometric phase has a spin-locking function, preventing independent control of left-hand or right-hand circularly polarized light. The purpose of spin decoupling is to break this lock, enabling the two circular polarization states to acquire arbitrary and mutually independent phase distributions. For a geometric phase metalens, when a left-handed circularly polarized light is incident on the metalens, the transmitted electric field can be described as follows:

$$E_{lcp}(x,y) = A\begin{bmatrix}1\\ i\end{bmatrix}\exp\left(i\varphi(x,y)\right) \tag{1}$$

Here, A represents the amplitude. To break the spin-locking effect caused by the geometric phase, an opposite phase term, -φ(x,y), is introduced into the metalens structure design. This allows for the simultaneous focusing and phase discretization of both left-handed and right-handed circularly polarized light, namely, $\phi(x,y) = \exp\left(i\varphi(x,y)\right) + \exp\left(-i\varphi(x,y)\right)$. This phase can achieve focusing on both left-handed and right-handed circularly polarized light. Here, if the incident light is linearly polarized, it exhibits both left-handed and right-handed circularly polarized light focusing phenomena.

The phase profile of the focusing metalens is expressed as:

$$\varphi(x,y) = -k\left(\sqrt{(x-x_0)^2+(y-y_0)^2+f^2} - \sqrt{x_0^2+y_0^2+f^2}\right) \tag{2}$$

where k is the wave vector, $k = 2\pi/\lambda$, λ is the wavelength, f is the focal length, and x_0 and y_0 denote the target focal position of the metalens. Based on the above spin-decoupling theory, the phase profile of the polarization-encoded multifocal metalens can be expressed as:

$$\varphi(x,y) = -k\left(\sum_{n=1}^{N_1}\sqrt{(x-x_0)^2+(y-y_0)^2+f^2}-\sqrt{x_0^2+y_0^2+f^2}\right) + k\left(\sum_{n=1}^{N_2}\sqrt{(x-x_0)^2+(y-y_0)^2+f^2}-\sqrt{x_0^2+y_0^2+f^2}\right) \quad (3)$$

where N_1 represents the number of focal spots generated for the left-handed circularly polarized light, and N_2 represents the number of focal spots generated for the right-handed circularly polarized light. The phase distribution calculation results of the multifocal metalens are shown in Supplementary Section 2.

Experimental Results

Metalens Characterization

Figure 2 shows the experimental results of the designed 4+8 multifocal metalens. This superlens utilizes the spin decoupling theory of geometric phase to encode left-handed and right-handed circularly polarized light into different focal channels, thereby achieving polarization-controllable multifocal generation. The experimental results show that under LCP, RCP, and linearly polarized incidence, the metalens can form 8, 4, and 12 focal spots, respectively, verifying its polarization selectivity and multifocal modulation capability of the device.

We constructed a transmission-type experimental setup, as shown in Figure 2(a). A 980 nm laser beam was converted into circularly polarized light using a linear polarizer and a quarter-wave plate. The beam was then focused onto the metalens sample using a 20× objective lens. The interaction between the beam and the metalens generated a focused light field. This focused light field was then collected again by the 20x objective lens, and after polarization filtering, the beam was acquired by a CCD. Experimentally results are shown in Figures 2(b)-(d). The lateral spacing between adjacent focal spots in the designed focal array is 35 μm, and the focal length is 200 μm. Figure 2(b) shows the intensity distribution of the focal plane under left-handed circularly polarized light incidence. It can be seen that eight clear focused light spots are formed on the focal plane, corresponding to the 8 focal points designed for the LCP channel in the metalens. This result indicates that the LCP channel can be effectively excited. Figure 2(c) shows the experimental results under right-handed circularly polarized light incidence. Four distinct focal spots are observed on the focal plane, corresponding to the 4 focal points designed for the RCP channel. Compared with the LCP case, the number and spatial position of the focal points change, indicating that the metalens exhibits a significant selective response to different circular polarization states. Figure 2(d) shows the intensity distribution of the focal plane under linearly polarized light incidence. Since linearly polarized light can be regarded as the superposition of left-handed circularly polarized and right-handed circularly polarized light, under this condition, the 8 focal points of the LCP channel and the 4 focal points of the RCP channel are simultaneously excited,

ultimately forming 12 focal points. This result further verifies the effectiveness of the 4+8 polarization encoding design.

To further evaluate the focusing quality of the focal points, we systematically characterized and analyzed their point spread function (PSF) and modulation transfer function (MTF). Figure 3(a) shows a magnified schematic diagram of the 12 focal spots generated under linearly polarized illumination, with the focal spots selected for PSF and MTF characterization highlighted by white dashed boxes. The first focus in the second row, x1-y2, is named focus number 2, and the third focus in the first row, x3-y1, is named focus number 9. For detailed focus numbering, please refer to Supplementary Section 3, which will facilitate subsequent quantitative analysis of parameters such as PSF, FWHM, and MTF of the focus. This figure illustrates that although there are certain intensity differences between the different focal spots, they can all form a well-quality focal spot overall. To better describe its transmission field distribution, a hundred images of different z-planes were acquired using an motorized translation stage for 3D reconstruction. Figure 3(b) shows the transmission field distribution near focal spot f = 200 μm. It can be seen that the optical field converges significantly near the focal plane and forms a high-intensity focal region at the focal plane. The dashed line indicates the focal plane, and the lateral intensity profile was used to extract the full width at half maximum (FWHM) of the focal spot. The experimentally measured FWHM of this focus is approximately 1.08 μm, indicating that the metalens possesses good focusing capability. Figure 3(c) and Figure 3(e) show the normalized PSF curves of focal spot 2 and focal spot 9, respectively. The blue curves represent the experimentally measured PSFs, the red curves represent the Gaussian fitting results, and the black dashed curves represent the theoretical Airy distributions. The measured PSF curve of focal spot 2 is better than that of focal spot 9. This is because focal spot 9 is located at the edge of the metalens, and the light intensity at the edge focus is relatively weak. Overall, the experimentally measured PSFs match the Gaussian fitting curves and the theoretical Airy distributions, indicating that the intensity distributions of the focal spots are close to the ideal focal spot profile. Figure 3(d) and Figure 3(f) show the MTF curves corresponding to focal spot 2 and focal spot 9, respectively. The MTF is used to characterize the ability of the system to transfer information at different spatial frequencies. The experimentally measured MTFs show good agreement with the Gaussian-fitted MTFs and the theoretical Airy MTFs, indicating that the spatial frequency response of the focal spots is close to the theoretical expectation and can support subsequent multifocal imaging and computational reconstruction. The main body of the paper focuses on the PSF and MTF analysis of focal spots 2 and 9, while Supplementary Section 3 analyzes the PSF and MTF of other focal spots. The PSF and MTF curves of the designed focal spots agree well with the theoretical Airy model and the Gaussian fitting results, indicating that the metalens not only enables polarization-multiplexed multifocal generation, but also exhibits good focusing quality and spatial frequency transmission capability.

To better characterize the polarization selectivity and channel crosstalk of the designed polarization-encoded metalens, the net integrated intensities of the designed focal regions under different polarization incidence were analyzed, and the corresponding polarization contrast was calculated. The polarization contrast is defined as the intensity ratio between the target polarization channel response and the orthogonal polarization crosstalk response, expressed as $C = 10\log10(I_{co}/I_{cro})$, and given in dB. Here, I_{co} and I_{cro} represent the net integrated intensities of the target polarization channel response and the orthogonal polarization crosstalk response,

197 respectively. The calculated polarization contrasts of the LCP and RCP channels are 20.75 dB and
198 20.14 dB, respectively, indicating that the metalens exhibits low polarization crosstalk and good
199 polarization selectivity.

200 **Multifocal Imaging with the Metalens**

201 The experimental results demonstrate that the designed 4+8 polarization-encoded metalens
202 achieves stable multi-focal point modulation across different polarization states, exhibiting low
203 polarization crosstalk and excellent focusing performance. Based on these results, a multifocal
204 imaging system was further constructed to perform imaging tests on a USAF 1951 resolution target,
205 thereby verifying the effectiveness of the metalens in imaging applications. Figure 4 shows a multi-
206 focal imaging experiment based on the polarization-multiplexed metalens. Figure 4(a) shows the
207 schematic of the imaging system. The laser beam is first collimated and polarization-modulated,
208 and then illuminates the USAF 1951 resolution target. The optical field transmitted through the
209 target is incident onto the designed polarization-multiplexed metalens, where the transmitted object
210 field is modulated into multiple focal channels. The images are collected by the rear imaging
211 objective and recorded by a CCD camera. The experimentally acquired multifocal images are
212 further processed through post-processing demixing and stitching to recover the target image.
213 Details of the USAF 1951 resolution target are shown in Figure S6 of Supplementary Section 4,
214 and the corresponding resolutions are listed in the table. Figure 4(b)-(d) show the raw multifocal
215 encoded images acquired under different polarization conditions. Since multiple focal channels
216 simultaneously participate in imaging, the raw images exhibit sub-image overlap, channel
217 crosstalk, and intensity nonuniformity, making it difficult to directly obtain a clear target image.
218 Therefore, information regarding the target pattern was obtained through image processing based
219 on the experimentally measured imaging results. Figure 4(e) shows the final reconstructed result,
220 in which the stripe patterns and numeral structures of elements 5 and 6 in group 5 of the resolution
221 target are clearly resolved. In addition, imaging results for element 1 of group 6 and elements 1 and
222 2 of group 7 are further provided in the Supplementary Material, achieving a resolution of 3.47 μm.
223 These results verify the feasibility of the designed metalens for multifocal imaging.
224 After the experimental imaging test of the USAF resolution target, the results demonstrate that the
225 designed 4+8 multifocal metalens can effectively image targets with regular high-contrast
226 structures, and clear images can be obtained through subsequent demixing, stitching, and
227 reconstruction. To further verify the applicability of the multifocal imaging model to complex
228 targets with continuous textures, microscopic images of onion epidermis were selected as the
229 imaging targets, and computational imaging validation was performed using the experimentally
230 measured 12-focal-spot PSF. Figure 5 shows the multifocal computational imaging results of the
231 onion epidermis based on the 12-focal-spot PSF. Figure 5(a) shows the overall computational
232 workflow. First, a target region O_{ROI} was selected from the microscopy image of the onion, while
233 the experimentally measured 12-focal-spot intensity distribution was used as the system point
234 spread function h_{12}. The physical pixel sizes of the onion image and the PSF image were used for
235 scale matching before convolution, ensuring that the target image and the PSF were placed on a
236 unified physical sampling grid. Subsequently, the target region was convolved with the complete
237 12-focal-spot PSF to obtain the multifocal encoded image:

$$I = O_{ROI} * h_{12} + n \tag{4}$$

where I represents the multifocal overlapped imaging result on the detection plane, and n denotes the noise term. Here, the 12 focal spots are treated as an integrated PSF in the convolution calculation; therefore, the field-of-view overlap and information mixing among different focal channels are naturally included in the encoded image. Subsequently, based on the known 12-focal-spot PSF, deconvolution/demixing reconstruction is performed on the encoded image to recover the target image O', and the error distribution between the reconstructed result and the original target region is calculated. Figure 5(b) shows the onion epidermal cell image observed under an optical microscope. Six regions were selected, among which regions 1 and 2 were used for computational imaging and reconstruction, as shown in Figures 5(c)–5(j). Figures 5(c) and 5(g) show the original cropped onion epidermal cell images of regions 1 and 2, respectively. Figures 5(d) and 5(h) show the results after convolution with the 12-focal-spot PSF. Due to image overlap, further demixing and stitching were performed to obtain the reconstructed images shown in Figures 5(e) and 5(i). The reconstructed images were subtracted from the original images to evaluate the reconstruction error, as shown in Figures 5(f) and 5(j). The relatively small errors indicate that the main texture orientations and grayscale structures of the onion epidermal cells were successfully recovered. The results for regions 3-6 are provided in Figure S8 of Supplementary Section 4. The computational imaging results demonstrate that the designed metalens can not only achieve multifocal optical-field modulation, but can also be combined with computational demixing and stitching methods to realize encoded imaging and reconstruction of complex biological sample images, providing a verification basis for subsequent multichannel super-resolution imaging applications.

Conclusion

In summary, we designed and experimentally verified an all-dielectric polarization-coded multifocal metalens, which realizes multifocal control and stitching imaging with polarization multiplexing. The designed metalens enables selective control over the number and spatial distribution of focal spots based on incident polarization states, generating 8, 4, and 12 focal spots under left-handed circular, right-handed circular, and linear polarization, respectively. Characterization via focusing properties, polarization contrast, point spread function (PSF), and modulation transfer function (MTF) demonstrates the device's excellent capabilities in optical field manipulation and imaging performance. Furthermore, by integrating multi-focal spot demixing and stitching algorithms, the method achieves the reconstruction of resolution chart images with a resolution of 3.47 μm and validates the feasibility of computational imaging for complex samples using onion epidermis images. The results indicate that this approach facilitates polarization multiplexing, multi-focal spot encoding, and field-of-view expansion within a compact optical architecture, offering a valuable reference for the application of metasurfaces in integrated biological microscopy and super-resolution imaging.

Data availability

The data that support the findings of this study are available from the corresponding authors upon reasonable request.

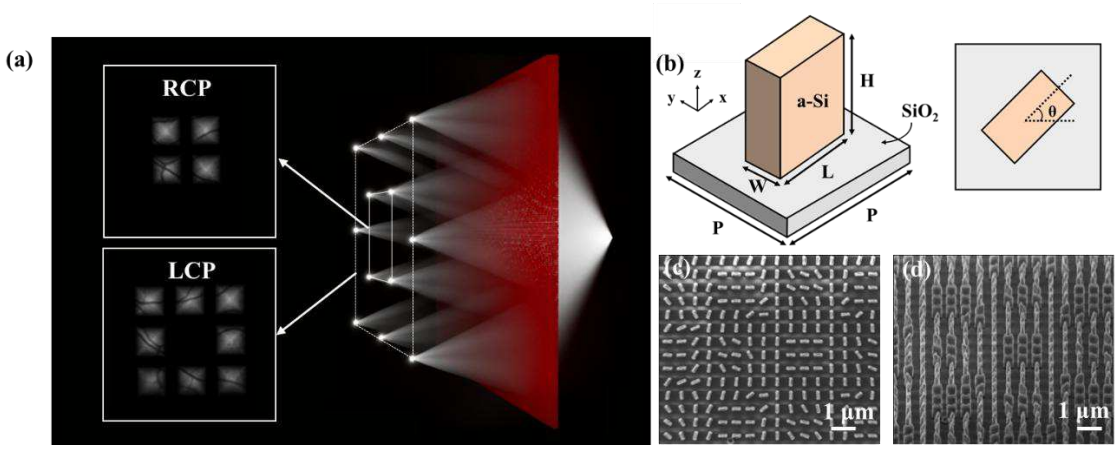


Figure 1. (a) Schematic diagram of polarization-encoded multifocal metalens. (b) Schematic of the structure. (c) Top-view SEM image. (d) Oblique-view SEM image.

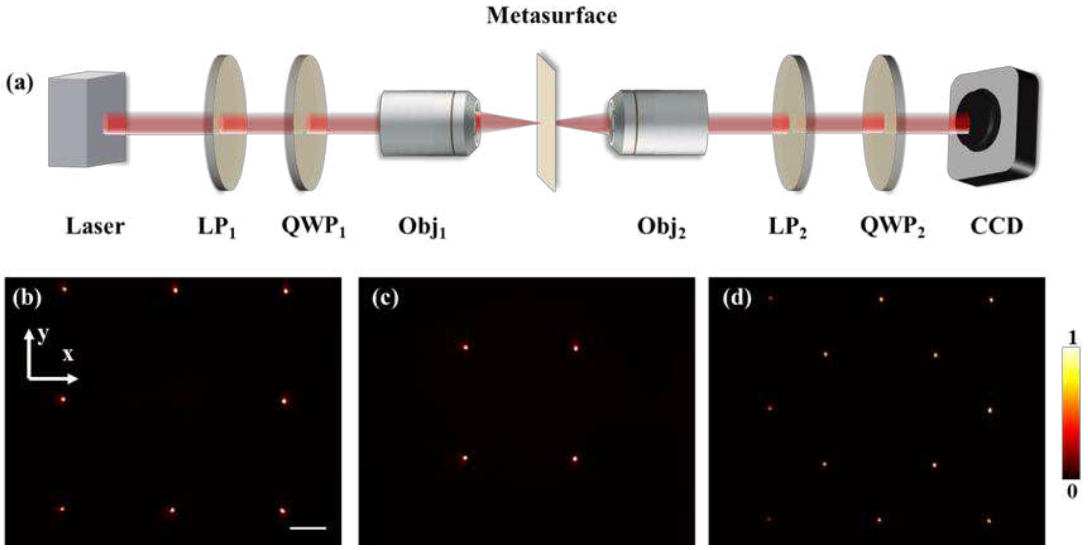


Figure 2. Experimental characterization of the polarization-encoded multifocal metalens. (a) Schematic diagram of the experimental setup. (b) Eight focal spots generated under under left-handed circularly polarized light incidence. (c) Four focal spots generated under under right-handed circularly polarized light incidence. (d) Twelve focal spots generated under linearly polarized light incidence. Scale bar: 10 μm.

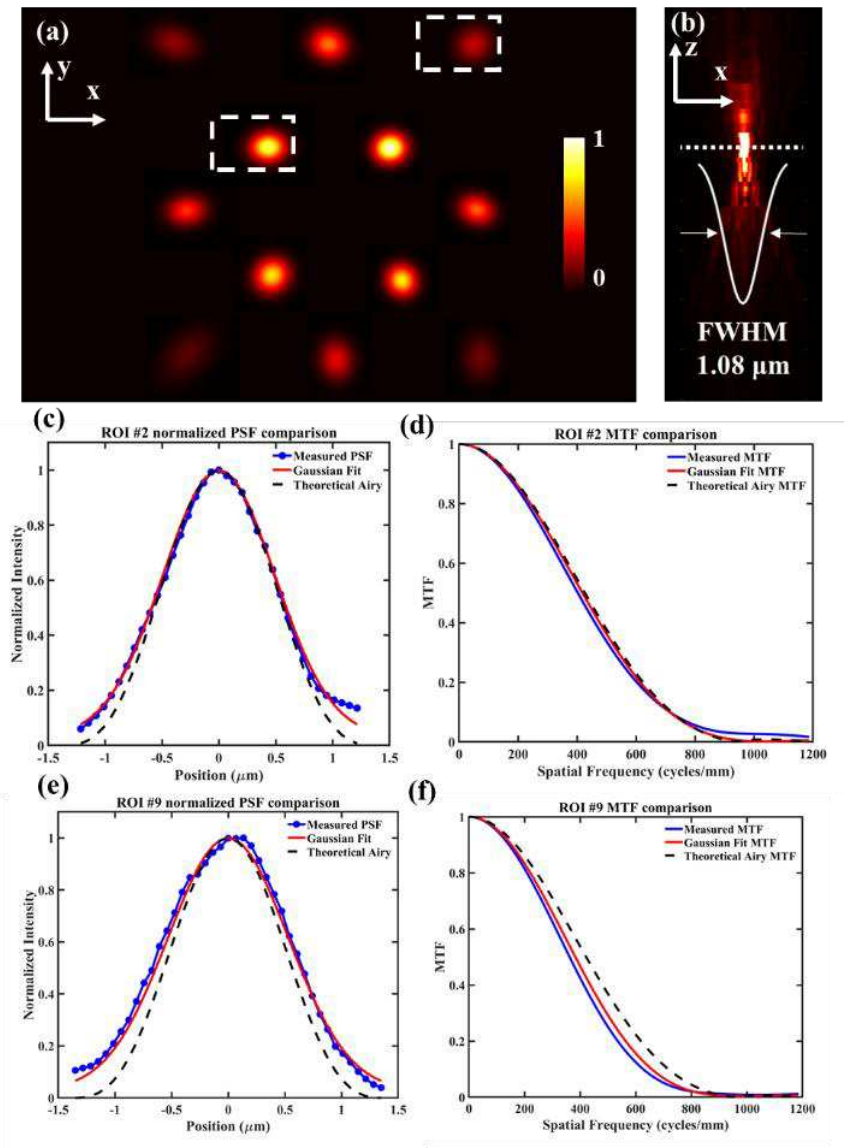


Figure 3. Experimental characterization of the PSFs and MTFs of the focal spots. (a) Enlarged views of the twelve focal spots. (b) Measured optical field distribution near focal Spot 2. (c)(e) normalized PSFs of focal spots 2 and 9, respectively. (d)(f) MTF curves of focal spots 2 and 9, respectively.

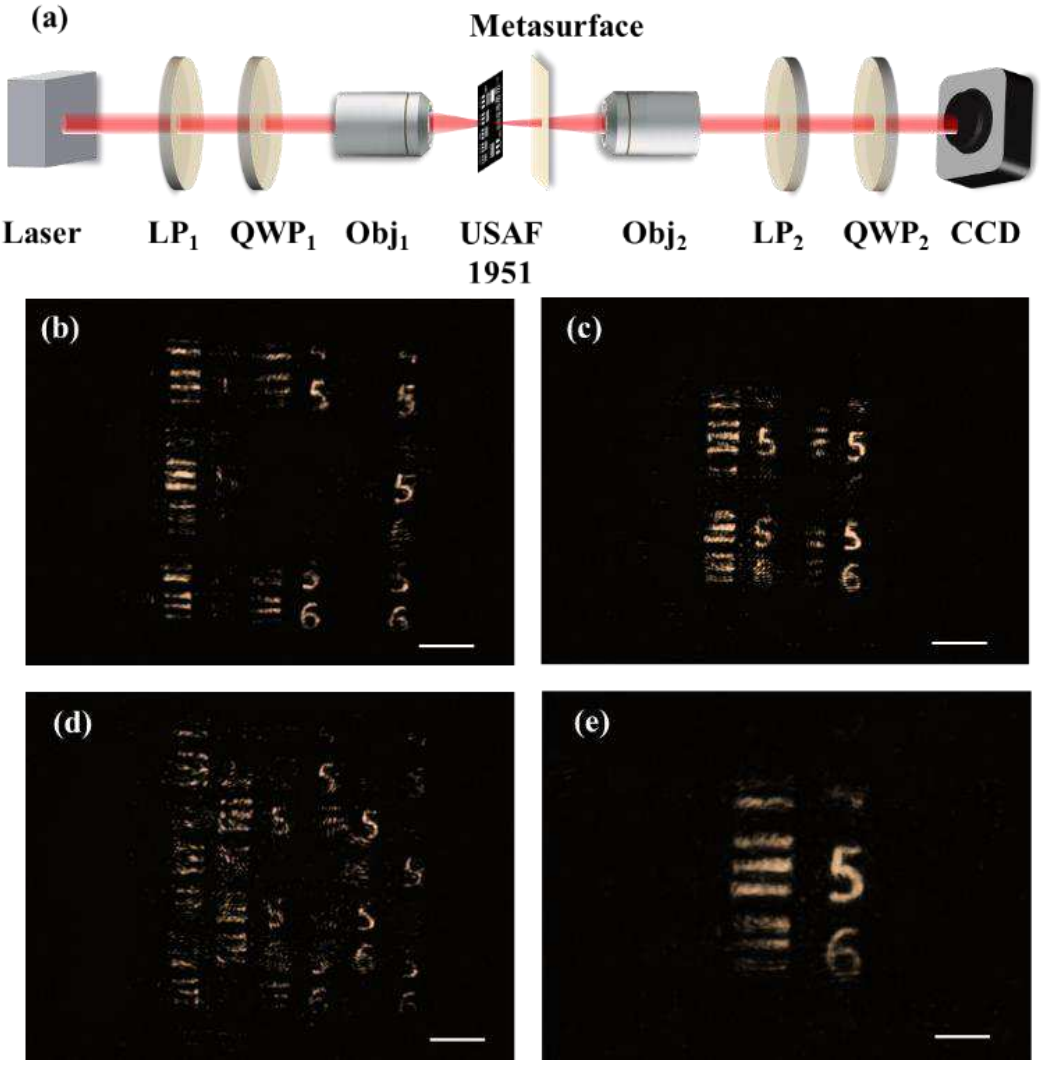


Figure 4. Resolution-target imaging experiment based on the 4+8 polarization-encoded multifocal metalens. (a) Schematic of the imaging system. (b) imaging result under LCP incidence. (c) imaging result under RCP incidence. (d) imaging result under LP incidence. (e) reconstructed imaging result. Scale bars: 100 μm in (b) and (d), and 40 μm in (c) and (e).

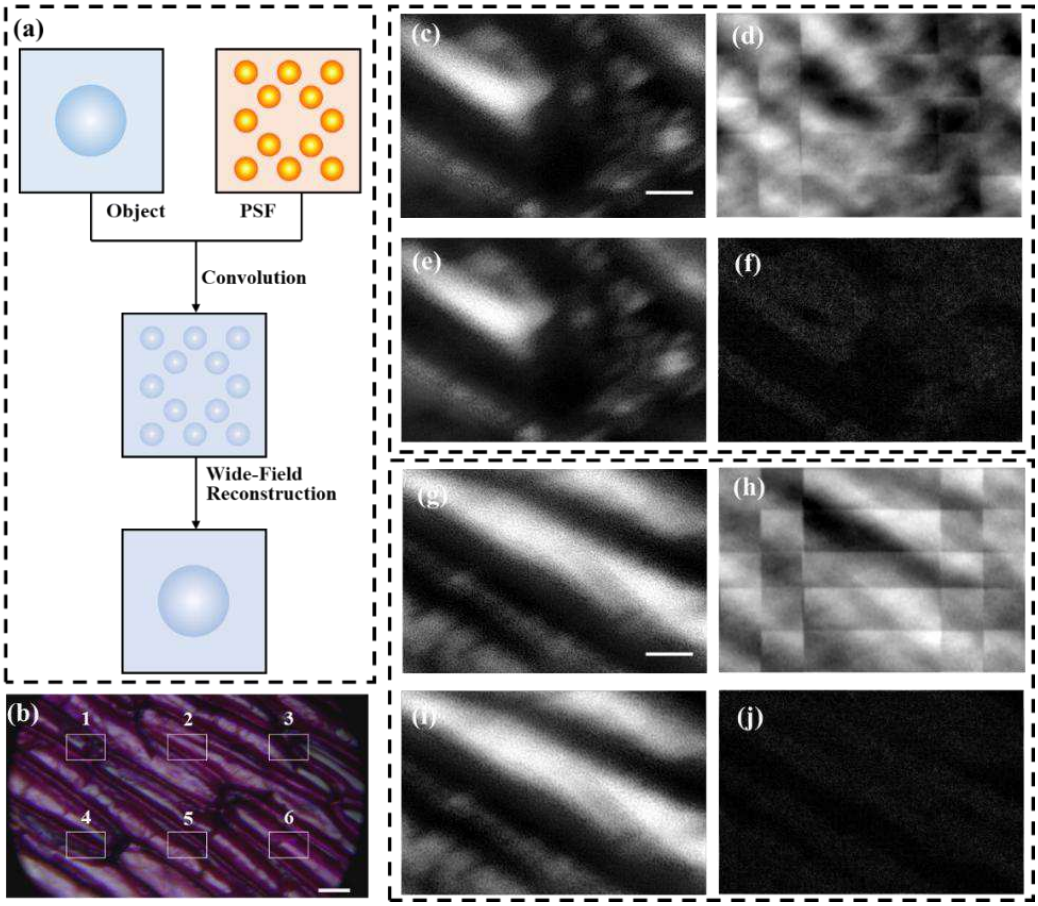


Figure 5. Computational imaging results of the polarization-encoded multifocal metalens. (a) Schematic illustration of the imaging principle. (b) original microscopic image of onion cells. (c)-(f) target-region image, PSF-convolved image, demixed and stitched reconstruction, and error map between the original and reconstructed images for region 1, respectively. (g)-(j) target-region image, PSF-convolved image, demixed and stitched reconstruction, and error map between the original and reconstructed images for region 2, respectively. Scale bar: 50 μm in (b) and 10 μm in (e)-(j).

REFERENCES AND NOTES

1. Yu, N. & Genevet, P. Light propagation with phase discontinuities: Generalized laws of reflection and refraction. Science 334, 333-337 (2011).
2. Kildishev, A. V., Boltasseva, A. & Shalaev, V. M. Planar photonics with metasurfaces. Science 339, 1232009 (2013).
3. Yu, N. & Capasso, F. Flat optics with designer metasurfaces. Nat. Mater. 13, 139-150 (2014).
4. Arbabi, A., et al. Subwavelength-thick lenses with high numerical apertures and large efficiency based on high-contrast transmitarrays. Nat. Commun. 6, 7069 (2015).
5. Khorasaninejad, M., et al. Metalenses at visible wavelengths: Diffraction-limited focusing and subwavelength resolution imaging. Science 352, 1190-1194 (2016).
6. Lin, D., et al. Dielectric gradient metasurface optical elements. Science 345, 298-302 (2014).
7. Arbabi, A., et al. Dielectric metasurfaces for complete control of phase and polarization with subwavelength spatial resolution and high transmission. Nat. Nanotechnol. 10, 937-943 (2015).
8. Devlin, R. C., et al. Broadband high-efficiency dielectric metasurfaces for the visible spectrum. PNAS 113, 10473-10478 (2016).
9. Genevet, P., et al. Recent advances in planar optics: From plasmonic to dielectric metasurfaces. Optica 4, 139-152 (2017).
10. Kamali, S. M., et al. A review of dielectric optical metasurfaces for wavefront control. Nanophotonics 7, 1041-1068 (2018).
11. Chen, W. T., et al. Flat optics with dispersion-engineered metasurfaces. Nat. Rev. Mater. 5, 604-620 (2020).
12. Aieta, F., et al. Multiwavelength achromatic metasurfaces by dispersive phase compensation. Science 347, 1342-1345 (2015).
13. Chen, W. T., et al. A broadband achromatic metalens for focusing and imaging in the visible. Nat. Nanotechnol. 13, 220-226 (2018).
14. Wang, S., et al. A broadband achromatic metalens in the visible. Nat. Nanotechnol. 13, 227-232 (2018).
15. Jeon, D., et al. Recent advancements of metalenses for functional imaging. Nano Convergence 10, 24 (2023).
16. Wang, X., et al. Advances in information processing and biological imaging using flat optics. Nat. Rev. Electr. Eng. 1, 391-411 (2024).
17. Khorasaninejad, M., et al. Multispectral chiral imaging with a metalens. Nano Lett. 16, 4595-4600 (2016).
18. Mueller, J. P. B., et al. Metasurface polarization optics: Independent phase control of arbitrary orthogonal states of polarization. Phys. Rev. Lett. 118, 113901 (2017).
19. Rubin, N. A., et al. Matrix Fourier optics enables a compact full-Stokes polarization camera. Science 365, eaax1839 (2019).
20. Rubin, N. A., et al. Polarization in diffractive optics and metasurfaces. Adv. Opt. Photon. 13, 836-970 (2021).
21. Xiong, B., et al. Breaking the limitation of polarization multiplexing in optical metasurfaces with engineered noise. Science 379, 294-299 (2023).
22. Arbabi, E., et al. Full-Stokes imaging polarimetry using dielectric metasurfaces. ACS Photonics 5, 3132-3140 (2018).
23. Zang, X., et al. A multi-foci metalens with polarization-rotated focal points. Laser Photonics Rev. 13, 1900182 (2019).
24. Zhou, T., et al. Helicity multiplexed terahertz multi-foci metalens. Opt. Lett. 45, 463-466 (2020).
25. Gao, S., et al. Twofold polarization-selective all-dielectric trifoci metalens for linearly polarized visible light. Adv. Opt. Mater. 7, 1900883 (2019).
26. Yao, Z. & Chen, Y. Focusing and imaging of a polarization-controlled bifocal metalens. Opt. Express 29, 3904-3914 (2021).
27. Wang, R., et al. Compact multi-foci metalens spectrometer. Light Sci. Appl. 12, 103 (2023).
28. Jiang, Z., et al. High-efficiency spin-selected multi-foci terahertz metalens. Opt. Lasers Eng. 174, 107816 (2024).
29. Wang, S., et al. Full Stokes polarimetry based on an inverse-designed multi-foci metalens. Opt. Lett. 49, 1595-1598 (2024).
30. Sun, C., et al. Nonclassical spin-multiplexing metasurfaces enabled multifunctional meta-scope. Small 20, 2404003 (2024).
31. Jo, Y., et al. Image scanning microscopy based on multifocal metalens for sub-diffraction-limited imaging of brain organoids. Light Sci. Appl. 14, 367 (2025).
32. Bosch, M., et al. Voltage-tunable multifunctional zoom imaging metalenses. ACS Photonics 12, 728-736 (2025).
33. Song, Y., et al. Inverse design of multiwavelength multifocal metalens based on the tandem neural networks. EPJ Appl. Metamater. 13, 13 (2026).

34. Che, X., et al. Varifocal Alvarez metalens array for adaptive light-field imaging. Nat. Commun. 17, 7882 (2026).
35. Colburn, S., et al. Metasurface optics for full-color computational imaging. Sci. Adv. 4, eaar2114 (2018).
36. Tseng, E., et al. Neural nano-optics for high-quality thin lens imaging. Nat. Commun. 12, 6493 (2021).
37. Zhou, Y., et al. NIR metalens achromatic imaging enabled by NAFGAN with physics-constrained training. Adv. Opt. Mater. 14, 2502400 (2026).

Acknowledgements

This work was supported by National Key Research and Development Program of China(2024YFA1409400), National Natural Science Foundation of China (No. 62305354 and No.62575294), and the Shanghai Sailing Program (No. 23YF1454100).

Author contributions

J.H. supervised project execution. X.S. and X.Y. conceived the study and designed the experiments. X.S. and X.Y. performed all measurements and analyses assisted by H.S., H.T., J.C., J.Z.. X.S. wrote and checked the manuscript. J.H. L.Z. and J.W. reviewed the manuscript. All authors commented on the paper.

Conflict of interest

Authors state no conflicts of interest.

Supplementary Files

This is a list of supplementary files associated with this preprint. Click to download.

- ManuscriptSi.docx